

Altermagnetic lifting of Kramers spin degeneracy

J. Krempaský,^{1,*} L. Šmejkal,^{2,3,*} S. W. D'Souza,^{4,*} M. Hajlaoui,⁵ G. Springholz,⁵
K. Uhlířová,⁶ F. Alarab,¹ P. C. Constantinou,¹ V. Stokov,¹ D. Usanov,¹
W. R. Pudelko,¹ R. González-Hernández,⁷ A. Birk Hellenes,² Z. Jansa,⁴
H. Reichlová,³ Z. Šobán,³ R. D. Gonzalez Betancourt,³ P. Wadley,⁸ J.
Sinova,^{2,3} D. Kriegner,³ J. Minár,^{4,†} J.H. Dil,⁹ and T. Jungwirth^{3,8,†}

¹*Photon Science Division, Paul Scherrer Institut, CH-5232 Villigen, Switzerland*

²*Institut für Physik, Johannes Gutenberg Universität Mainz, D-55099 Mainz, Germany*

³*Institute of Physics, Czech Academy of Sciences,
Cukrovarnická 10, 162 00 Praha 6 Czech Republic*

⁴*University of West Bohemia, New Technologies
Research Center, Plzen 30100, Czech Republic*

⁵*Institute of Semiconductor and Solid State Physics,
Johannes Kepler University Linz, 4040 Linz, Austria*

⁶*Faculty of Mathematics and Physics, Charles University,
Ke Karlovu 3, CZ-121 16, Prague 2, Czech Republic*

⁷*Grupo de Investigación en Física Aplicada, Departamento de Física,
Universidad del Norte, Barranquilla, Colombia*

⁸*School of Physics and Astronomy, University of Nottingham,
Nottingham NG7 2RD, United Kingdom*

⁹*Institut de Physique, École Polytechnique Fédérale
de Lausanne, CH-1015 Lausanne, Switzerland*

Lifted Kramers spin-degeneracy has been among the central topics of condensed-matter physics since the dawn of the band theory of solids [1, 2]. It underpins established practical applications as well as current frontier research, ranging from magnetic-memory technology [3–7] to topological quantum matter [8–17]. Traditionally, lifted Kramers spin-degeneracy has been considered to originate from two possible internal symmetry-breaking mechanisms. The first one refers to time-reversal symmetry breaking by magnetization of ferromagnets, and tends to be strong due to the non-relativistic exchange-coupling origin [18]. The second mechanism applies to crystals with broken inversion symmetry, and tends to be comparatively weaker as it originates from the relativistic spin-orbit coupling [19–22]. A recent theory work based on spin-symmetry classification has identified an unconventional magnetic phase, dubbed *altermagnetic* [23, 24], that allows for lifting the Kramers spin degeneracy without net magnetization and inversion-symmetry breaking. Here we provide the confirmation using photoemission spectroscopy and *ab initio* calculations. We identify two distinct unconventional mechanisms of lifted Kramers spin degeneracy generated by the *altermagnetic* phase of centrosymmetric MnTe with vanishing net magnetization [23–26]. Our observation of the *altermagnetic* lifting of the Kramers spin degeneracy can have broad consequences in magnetism. It motivates exploration and exploitation of the unconventional nature of this magnetic phase in an extended family of materials, ranging from insulators and semiconductors to metals and superconductors [23, 24], that have been either identified recently or perceived for many decades as conventional antiferromagnets [24, 27, 28].

A recently developed spin-symmetry classification focusing on collinear magnets and, within the hierarchy of interactions, on the strong non-relativistic exchange, has identified a third elementary type of magnetic phases in addition to the conventional ferromagnets and antiferromagnets [23, 24]. The exclusively distinct spin-symmetry characteristics of this emerging third, *altermagnetic* class are the opposite-spin sublattices connected by a real-space rotation transformation (proper or improper and symmorphic or non-symmorphic), but not connected by a translation or inversion [23, 24]. In contrast, the conventional

* These three authors contributed equally

† Corresponding authors: juraj.krempasky@psi.ch, jminar@ntc.zcu.cz, jungw@fzu.cz

ferromagnetic (ferrimagnetic) class has one spin lattice or opposite-spin sublattices not connected by any symmetry transformation, and the conventional antiferromagnetic class has opposite-spin sublattices connected by a real-space translation or inversion. For the case of inversion, the Kramers spin degeneracy of bands in these conventional antiferromagnets is protected even in the presence of the relativistic spin-orbit coupling [29]. For the translation connecting the opposite-spin sublattices, lifting of the Kramers spin degeneracy in these antiferromagnets requires both spin-orbit coupling and inversion-symmetry breaking in the crystal, in analogy to ordinary non-magnetic systems.

The unconventional nature of altermagnets is that the rotation symmetry connecting the opposite-spin sublattices protects an antiferromagnetic-like compensated magnetic order with a vanishing net magnetization while, simultaneously, it enables a ferromagnetic-like lifting of the Kramers spin degeneracy without breaking the crystal inversion symmetry and without additional symmetry breaking by the relativistic spin-orbit coupling [23, 24]. Here we will refer to this mechanism as "strong" altermagnetic lifting of the Kramers spin degeneracy.

Apart from the signature antiferromagnetic-like vanishing magnetization and ferromagnetic-like strong spin-degeneracy lifting, whose presence have been traditionally considered as mutually exclusive in one physical system, altermagnets can host a range of novel phenomena that are unparalleled in either the conventional ferromagnets or antiferromagnets [23, 24]. Within the realm of (lifted) Kramers spin-degeneracy physics, a unique property associated with the alternating sign of the spin polarization in the altermagnet's Brillouin zone is the presence of an even number of spin-degenerate nodal surfaces crossing the zone-center (Γ -point) in the non-relativistic band structure. In Fig. 1a we demonstrate that these spin degeneracies can be lifted by the relativistic spin-orbit coupling in altermagnets even without breaking the crystal inversion symmetry. We will refer to this mechanism as "weak" altermagnetic lifting of the Kramers spin degeneracy. A comparison of these unconventional weak and strong mechanisms of lifted Kramers spin degeneracy, enabled by altermagnetism, are illustrated in Figs. 1a,b.

Both the strong and the weak altermagnetic lifting of the Kramers spin degeneracy can enrich fields ranging from spintronics, ultrafast magnetism, magneto-electrics and magnonics, to topological matter, dissipationless quantum nanoelectronics and superconductivity [23, 24]. For example, the strong altermagnetic lifting of the Kramers spin degeneracy

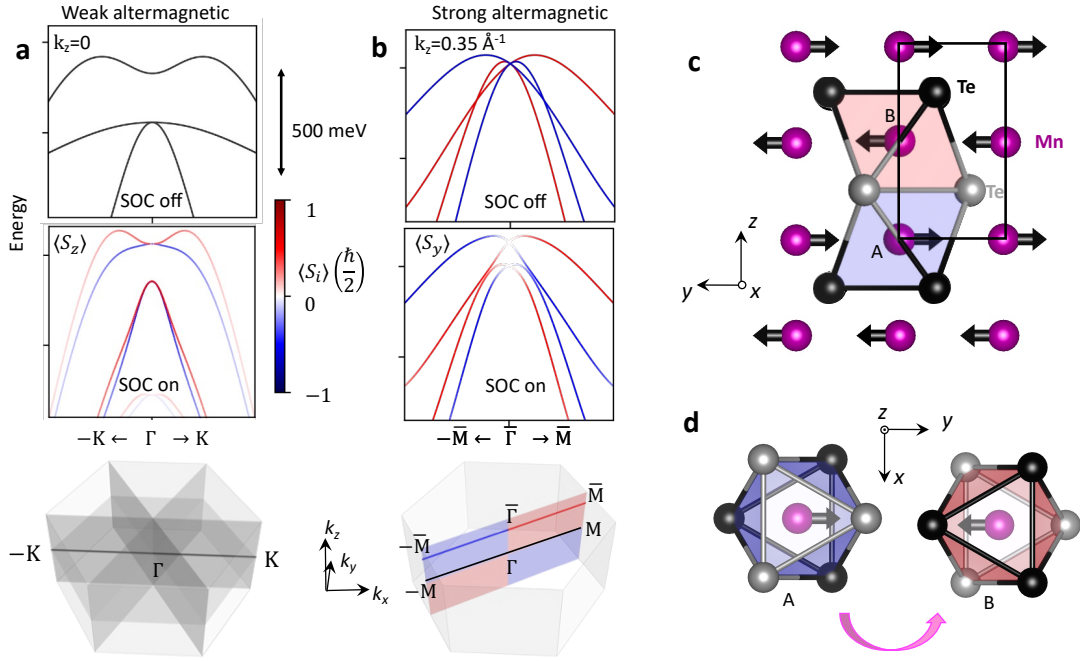


Fig. 1. Illustration of weak and strong altermagnetic lifting of Kramers spin degeneracy. **a**, Top and middle panels: *ab initio* band structure of MnTe at $k_z = 0$ along the $\Gamma - \mathbf{K}$ path for relativistic spin-orbit coupling turned off and on, resp. Néel vector is along the crystal y -axis (see panels c,d), corresponding to the $\Gamma - \mathbf{M}$ axis (see bottom panel of **b**). Red and blue colors correspond to opposite z -components of spin. Bottom panel: Schematics of the Brillouin zone with four spin-degenerate nodal planes in the electronic structure with spin-orbit coupling turned off. **b**, Same as **a** at $k_z = 0.35 \text{ \AA}^{-1}$ along the $\bar{\Gamma} - \bar{\mathbf{M}}$ path illustrating the strong altermagnetic lifting of Kramers spin degeneracy. Red and blue colors correspond to opposite y -components of spin. Bottom panel highlights the $\bar{\Gamma} - \bar{\mathbf{M}}$ path outside the four nodal planes (the red and blue colors highlight the alternating symmetry of the spin polarization in the plane). **c,d** Schematic view of the crystal and magnetic structure of MnTe in the $y - z$ and $x - y$ plane, resp. The red and blue shadings in **c,d** mark Te-octahedra around the Mn sites A and B with opposite spins which are related by spin rotation combined with six fold crystal rotation and half-unit cell translation along the z -axis.

has been theoretically shown to enable analogous spin-polarized currents to those used for reading and writing information in ferromagnetic memory devices while, simultaneously, removing the capacity and speed limitations imposed by a net magnetization [23, 24, 30–34].

The weak altermagnetic lifting of the Kramers spin degeneracy has been linked to Berry-phase physics governing the dissipationless anomalous Hall currents while, again, removing the roadblocks associated with magnetization for realizing robust quantum-topological variants of these effects [17, 24, 25, 35–40]. Several of the predicted unconventional macroscopic time-reversal symmetry breaking responses accompanied by the vanishing magnetization have been already experimentally confirmed in altermagnetic RuO₂ or MnTe [25, 41–44]. Here, using angle-resolved photoemission spectroscopy, we directly identify the weak and strong altermagnetic lifting of the Kramers spin degeneracy in the band structure of MnTe.

A schematic crystal structure of α -MnTe is shown in Fig. 1c,d. The two crystal sublattices A and B of Mn atoms, whose magnetic moments order antiparallel below the transition temperature of 310 K, are connected by a non-symmorphic six-fold screw-axis rotation, and are not connected by a translation or inversion [23, 25]. The resulting non-relativistic electronic structure of this altermagnet is of the g -wave type [23] with three spin-degenerate nodal planes parallel to the k_z -axis and crossing Γ and \mathbf{K} points, and one additional spin degenerate nodal plane orthogonal to the k_z -axis and crossing the Γ point ($k_z = 0$ nodal plane). These four nodal planes are highlighted in the bottom panel of Fig. 1a.

Angle-resolved photoemission spectroscopy (ARPES) measurements, shown in Fig. 2, were performed within the $k_z = 0$ nodal plane along k_x ($\Gamma - \mathbf{K}$ path) and k_y ($\Gamma - \mathbf{M}$ path) using an X-ray photon energy of 667 eV. The experiments were performed on the soft X-ray ARPES beamline ADDRESS at the Swiss Light Source synchrotron facility [45, 46]. Samples used in these measurements are thin MnTe films grown by molecular-beam epitaxy on a single-crystal InP(111)A substrate [25, 47]. We used a vacuum suitcase to transfer the thin-film samples from the growth to the soft X-ray ARPES chamber without breaking ultra-high-vacuum conditions (for details on the sample growth and characterization, and on the measurement techniques see Methods).

In Fig. 2a we show the measured raw data along the k_x -axis (bottom panel) and compare with one-step simulation of the photoemission process (top panel), using the Korringa-Kohn-Rostoker *ab-initio* approach that represents the electronic structure in terms of single-particle Green’s functions [48, 49]. The intense spectral weight around -3.5 eV binding energy, indicated by a magenta dashed line in the experimental and theoretical panels of Fig. 2a, corresponds to a resonance due to Mn d-states. For a better visualization of the bulk electronic structure of MnTe, this spectral weight is filtered out in the experimental ARPES band

maps shown in Figs. 2b,c. Refinements by the curvature mapping [50] extracted from the area highlighted by a white-dashed rectangle are shown in insets of top panels of Figs. 2b,c. These are compared to the corresponding relativistic *ab-initio* electronic structure calculations plotted in the bottom panels of Figs. 2b,c. The theoretical bands, with red and blue colors depicting opposite spin polarizations along the z -axis, show the weak altermagnetic lifting of the Kramers spin degeneracy within the $k_z = 0$ nodal plane. The relativistic band-structure calculations were performed assuming the Néel vector along the in-plane y -axis (see Fig. 1c), consistent with earlier magnetic and magneto-transport measurements of the Néel-vector easy axis in epitaxial thin films of MnTe [25, 51]. Altermagnetism and spin-orbit coupling thus generate in this case an unconventional spin polarization of bands that is orthogonal to the direction of the magnetic-order vector.

The experimental ARPES band maps in Figs. 2b,c are fully consistent with the *ab-initio* band structures. This includes the overall band dispersions, as well as the significantly larger splitting of the top two bands along the k_x -axis ($\Gamma - \mathbf{K}$ path, Fig. 2b) than along the k_y -axis ($\Gamma - \mathbf{M}$ path, Fig. 2c). The splitting is highlighted in Fig. 2b by the red double-arrow in the experimental curvature map, and the two split bands have opposite spins in the corresponding *ab-initio* band structure. We again emphasize that this weak altermagnetic lifting of the Kramers spin degeneracy requires relativistic spin-orbit coupling and is unconventional as it is observed in the bulk band structure of an inversion-symmetric crystal. The extraordinary spin-splitting magnitude ~ 100 meV and the quadratic dispersion around the Γ -point (see also Fig. 3c), consistently observed in experiment and theory, further highlight the unconventional nature of this lifting of the Kramers spin degeneracy in altermagnetic MnTe.

Fig. 2d shows a $k_z = 0$ constant-energy map measured at the X-ray photon energy of 667 eV, obtained by integrating the measured data over a 50 meV interval of binding energies from the top of the valence band. The observed 6-fold symmetry indicates that within the probing area of this ARPES measurement, there is a comparable population of three Néel-vector easy axes, corresponding to the $\Gamma - \mathbf{M}_{1-3}$ axes, that are crystallographically equivalent in the ideal hexagonal lattice of MnTe. Our observation of a multi-domain state is consistent with earlier magnetotransport measurements of the MnTe epilayers [25, 47]. We point out that domains with all these three Néel-vector easy axes exhibit larger spin splitting along $\Gamma - \mathbf{K}_{1-3}$ paths than along $\Gamma - \mathbf{M}_{1-3}$ paths, as shown in Extended Data

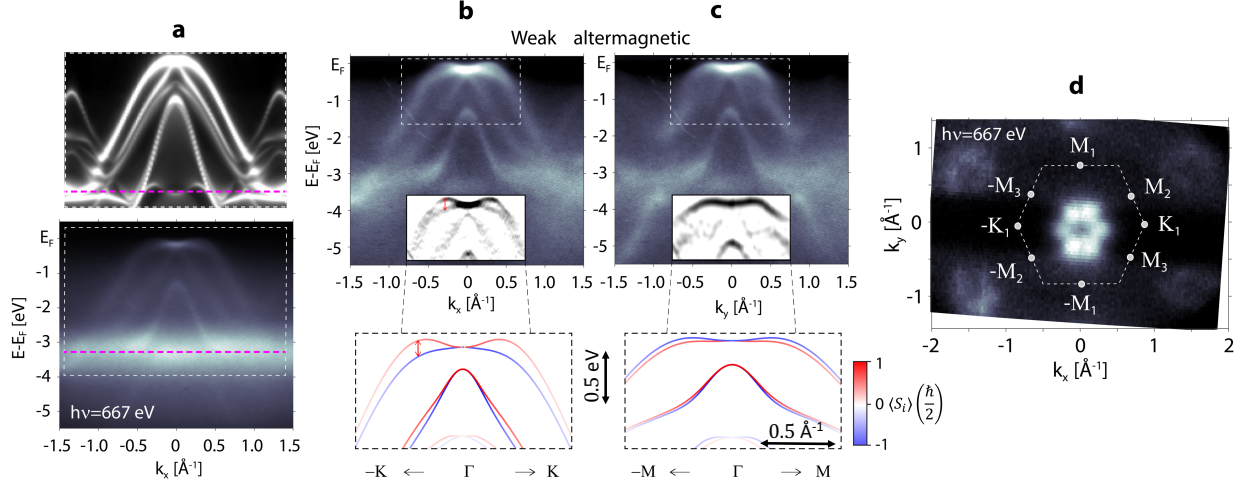


Fig. 2. **Weak altermagnetic lifting of Kramers spin degeneracy in the nodal plane.** **a**, Bottom panel: Measured soft X-ray (667 eV) ARPES band map at $k_z = 0$ along k_x ($\Gamma - \mathbf{K}$ path) on epitaxial thin-film MnTe. Top panel: Corresponding one-step ARPES simulation. Magenta dashed line highlights an intense spectral weight around -3.5 eV binding energy corresponding to a resonance of Mn d-states. **b**, Measured ARPES band map along k_x ($\Gamma - \mathbf{K}_1$ path) after filtering out the intense spectral weight due to the Mn d-state resonance. Inset: Refinement of the measured data by curvature mapping. Bottom panel: *Ab initio* bands with red and blue colors corresponding to opposite z -components of spin. The Néel vector is aligned along the $\Gamma - \mathbf{M}_2$ direction in the calculations. **c**, Same as **b** along k_y ($\Gamma - \mathbf{M}_1$ path). **d**, Constant-energy map obtained by integrating the measured data over a 50 meV binding-energy interval from the top of the valence band.

Fig. 1. Therefore, even when the population of the three domains is comparable within the sample probing area (X-ray spot position), a significantly larger splitting is expected for the $\Gamma - \mathbf{K}_{1-3}$ paths than for the $\Gamma - \mathbf{M}_{1-3}$ paths. This corroborates the excellent agreement between the experimentally observed and the calculated band splittings in Fig. 2b,c.

The top-left panel of Fig. 3a shows the refinements by the curvature mapping corresponding to Fig. 2d. Together with the one-step ARPES simulation assuming an equal population of the three easy axes, shown in the top-right panel of Fig. 3a, it confirms the 6-fold symmetry of this constant-energy cut. In the series of panels in Fig. 3a, we then systematically explore the symmetry of the constant-energy maps measured and calculated at different binding energies, indicated by symbols A-D in the band dispersion shown in Fig. 3c.

Analogous set of measurements and calculations is shown in Fig. 3b for a different probing area on the sample (different X-ray spot position). While the maps in Fig. 3a show the 6-fold symmetry for all binding energies, the maps in Fig. 3b have a lower 2-fold symmetry at energies near the top of the valence band (binding energies A-C). The 6-fold symmetry is observed in Fig. 3b only deeper in the valence band (binding energy D). The one-step ARPES simulations in Fig. 3b were performed assuming a single-domain state with the Néel vector along the easy axis corresponding to the $\Gamma - \mathbf{M}_1$ axis. The agreement between experiment and theory for all the studied constant-energy maps confirms that in the probing area of the MnTe epilayer corresponding to Fig. 3b, there is a prevailing population of one of the three Néel-vector easy-axis domains ($\Gamma - \mathbf{M}_1$ axis). A comparison to another probing area on the sample with an intermediate domain-population character between those of Figs. 3a,b is shown in Extended Data Fig. 2. Note that, in Fig. 3b, the more prominent lowering of the symmetry from 6 to 2-fold near the top of the valence band correlates with the dominant contribution of p -orbitals of the heavy Te atoms, which significantly enhances the strength of spin-orbit coupling in this spectral range (see Extended Data Fig. 3).

As explained in the introduction and illustrated in Fig. 1, the strong altermagnetic lifting of the Kramers spin degeneracy can be identified in the electronic structure only outside the four nodal planes that are spin-degenerate in the non-relativistic limit. In Fig. 4 we compare the measured and simulated ARPES data inside and outside the nodal planes. Soft X-ray ARPES band maps for $k_z = 0.35 \text{ \AA}^{-1}$ (X-ray photon energy of 368 eV) along a path parallel to $\Gamma - \mathbf{K}$, i.e., within one of the nodal planes, are shown in Figs. 4a,b. To highlight the finite k_z value, we label the path as $\bar{\Gamma} - \bar{\mathbf{K}}$. Data for the same k_z value and a path $\bar{\Gamma} - \bar{\mathbf{M}}$, i.e., outside the nodal planes, are shown in Figs. 4c,d. In both experiment and theory, we observe a significantly larger band splitting in Figs. 4c,d (strong altermagnetic), reaching a half-eV scale, than Figs. 4a,b (weak altermagnetic) in the part of the spectrum labeled by B_1 and B_2 . The spin-resolved one-step ARPES simulations of this part of the spectrum then suggest that a sizable spin-polarization signal should be detectable by spin-resolved ARPES (SARPES). This applies in particular to the $\bar{\Gamma} - \bar{\mathbf{M}}$ path featuring the strong altermagnetic lifting of the spin degeneracy.

The spin-resolved measurements were performed on the UV SARPES end-station COPHEE at the Swiss Light Source [52]. Since the COPHEE sample holder was not compatible with the Omicron plate used in the vacuum suitcase, and the system did not allow for decapping

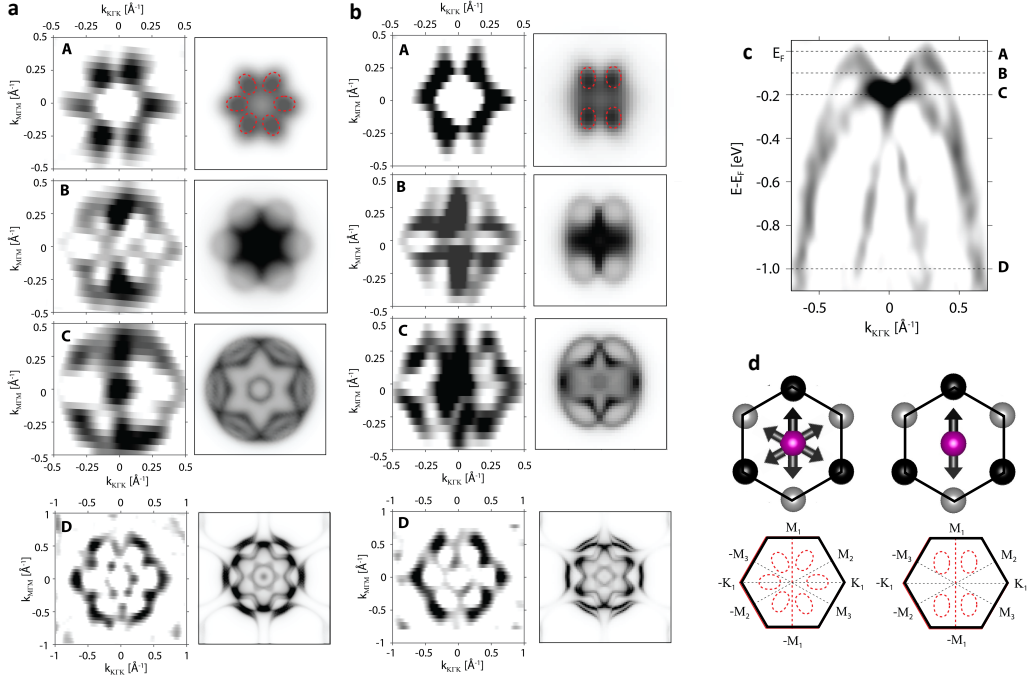


Fig. 3. Constant-energy maps and Néel-vector easy-axis domains. **a**, Left column: Refinements by the curvature mapping of measured constant-energy maps for binding energies A-D indicated in panel **c**. Right column: Corresponding one-step ARPES simulations. **b**, Same as **a** for a different probing area on the sample (different X-ray spot position). Dashed red contours highlight the 6-fold (2-fold) symmetry in top right panels of **a** (**b**). **c**, Refinement by the curvature mapping of the band map from the main experimental panel of Fig. 2a at $k_z = 0$ along the $\Gamma - \mathbf{K}$ path with the indicated binding energies A-D. **d**, Schematics of the 6-fold symmetry of constant-energy maps (bottom-left) for an equal (comparable) population of the three Néel-vector easy axes (top-left), and a lowered 2-fold symmetry of constant-energy maps (bottom-right) for one of the three easy-axis domains prevailing (top-right).

the MnTe surface, we performed the SARPES measurements on *in situ* cleaved bulk-crystal samples. The bulk single crystals of MnTe were grown using the self-flux method. Their structural quality was confirmed by X-ray diffraction. Magnetization measurements by a superconducting quantum interference device verified the compensated magnetic ordering with the Néel temperature at 310 K and the Néel vector in the z -plane, consistent with earlier reports on bulk crystals [28], and also consistent with the magnetic characteristics of our thin MnTe films. (For more details on the characterization of the bulk MnTe crystals

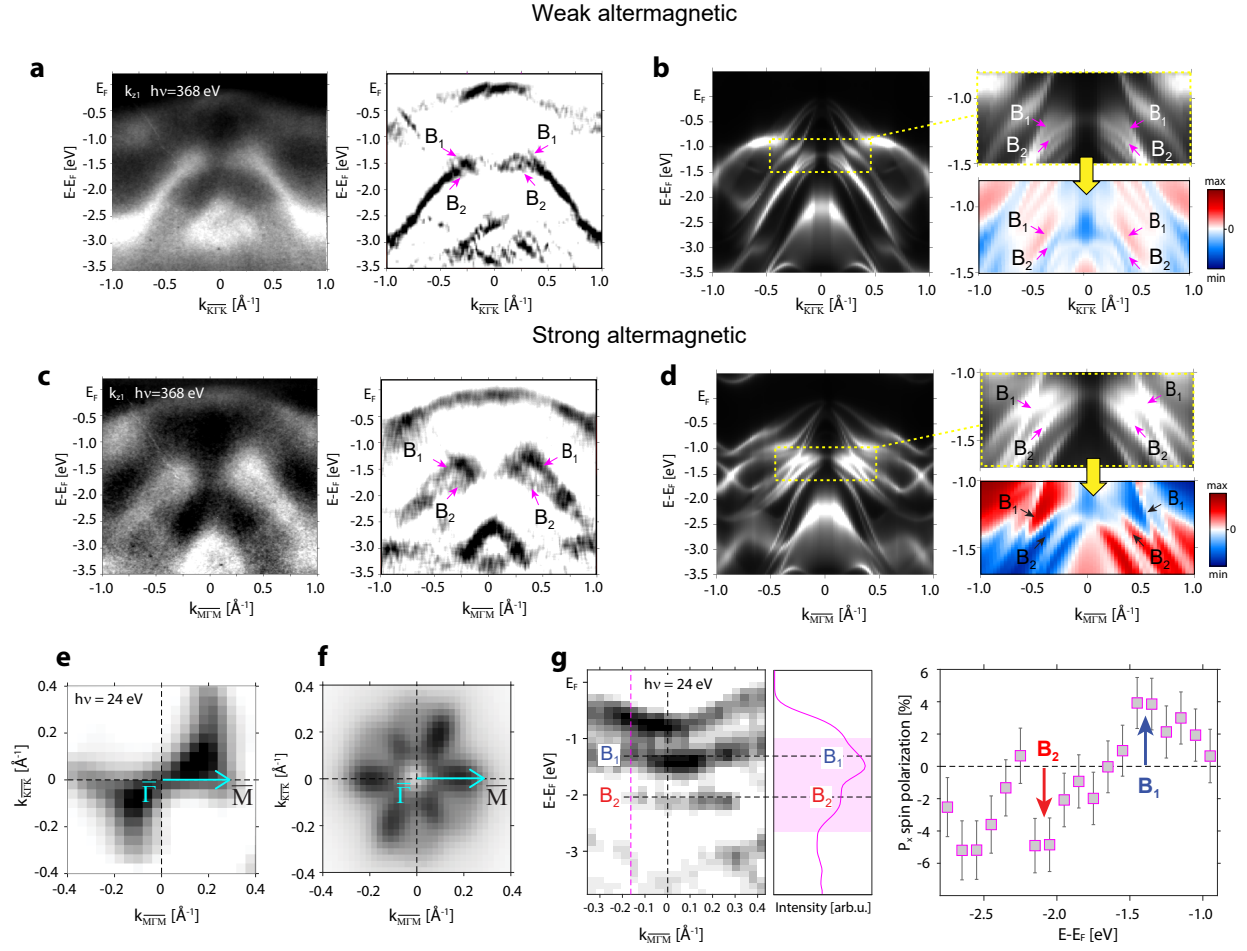


Fig. 4. **Weak and strong lifting of Kramers spin degeneracy at $k_z \neq 0$.** **a**, Measured soft X-ray (368 eV) ARPES band map at $k_z = 0.35 \text{ \AA}^{-1}$ along the $\bar{\Gamma} - \bar{K}$ path (left: unrefined data, right: refined data). **b**, Corresponding one-step ARPES simulations. Red and blue colors show opposite y -components of spin. **c,d** Same as **a,b** along the $\bar{\Gamma} - \bar{M}$ path. **e**, Experimental UV (24 eV) ARPES constant-energy maps at $k_z = 0.12 \text{ \AA}^{-1}$ measured on bulk-crystal MnTe. **f**, Corresponding one-step UV ARPES simulations. **g**, Experimental UV ARPES band map along the $\bar{\Gamma} - \bar{M}$ path (left), corresponding total-intensity energy-distribution curve (middle) and SARPES (right). The spin polarization is detected along the $\bar{\Gamma} - \bar{M}$ axis. In all theoretical panels, the considered Néel vector and the spin-polarization projection are along an axis corresponding to the $\bar{\Gamma} - \bar{M}_1$ axis (also highlighted by the cyan arrow in panels e,f), and the considered paths are $\bar{\Gamma} - \bar{K}_1$ and $\bar{\Gamma} - \bar{M}_1$.

see Methods and Supplementary information.)

The consistency between the electronic structures of the MnTe thin-film and bulk-crystal samples is illustrated on soft X-ray ARPES band maps shown in Extended Data Figs. 3a,b, accompanied by the corresponding one-step ARPES simulations in Extended Data Figs. 3c. (Note that in both the experimental and theoretical band maps we consistently observe that the photoemission final state effects almost completely suppress the band mapping for Γ_2 and Γ_4 .) The colored stripes in experimental panels of Extended Data Fig. 3 highlight resonances due to Te-states (purple) and Mn-states (yellow-green), also observed in the simulations. In Extended Data Fig. 3d,e we accompany the ARPES data by plotting corresponding atomic-orbital projections of *ab initio* bands and the density of states, consistently showing that the Te *p*-orbitals dominate the top of the valence band, while the spectral weight of Mn *d*-orbitals becomes significant below -3 eV.

UV ARPES measurements of the MnTe bulk crystal at photon energy of 24 eV and the corresponding simulation of the constant energy map for non-zero k_z ($k_z = 0.12 \text{ \AA}^{-1}$) are shown in Figs. 4e,f. The lowered 2-fold symmetry confirms the prevailing population of one of the three easy-axis domains in the probing area of the measured bulk-crystal sample. In the UV ARPES band map along the $\bar{\Gamma} - \bar{\text{M}}$ path, plotted in the left panel of Fig. 4g, we identify the analogous spectral features to those labelled as B₁ and B₂ in Figs. 4c,d whose expected spin polarization is due to the strong altermagnetic lifting of the Kramers spin degeneracy. The spin polarization is experimentally confirmed by the UV SARPES measurements in Fig. 4g. In the middle panel of Fig. 4g we plot the measured total-intensity energy-distribution curve (EDC), and the corresponding SARPES signal is shown in the right panel of Fig. 4g. As expected, we observe the alternating sign of the spin-polarization component along the Néel vector, consistent with the presence of the strong altermagnetic lifting of the Kramers spin degeneracy for the $\bar{\Gamma} - \bar{\text{M}}$ path.

In conclusion, we have observed two types of unconventional lifting of Kramers spin degeneracy in altermagnetic MnTe. The weak altermagnetic mechanism generates extraordinary relativistic spin-splitting magnitude ~ 100 meV and quadratic dispersion around the Γ -point. The strong altermagnetic mechanism in the magnetically compensated and centrosymmetric MnTe reaches a remarkable half-eV scale. The experimental observations are in excellent agreement with *ab initio* calculations. The agreement between the spin-split band structure observed in ARPES and obtained from density-functional theory confirms the prediction [24, 34] that altermagnetism can originate directly from crystal

symmetries, without requiring strong electronic correlations. Specifically, it confirms that altermagnetism stems from the local crystal anisotropy that breaks translation and inversion symmetry but preserves a rotation symmetry connecting the opposite-spin sublattices. The crystal-symmetry basis makes altermagnetism one of the elementary phases of matter which, remarkably, has been omitted for nearly a century of the band theory of solids. Our results highlight the strength of the spin-group symmetry classification in unraveling new magnetic phases and in describing the hierarchy of energy scales that underpin their rich phenomenology and potential applications [17, 24, 34].

METHODS

Thin film growth. MnTe epilayers of 200 nm thickness were grown by molecular beam epitaxy on single crystalline In-terminated InP(111) substrates using elemental Mn and Te sources. The less than 1% lattice mismatch results in single crystalline hexagonal MnTe growth with the c -axis (z -axis) perpendicular to the surface. Two-dimensional growth of α -MnTe is achieved at substrate temperatures of 370–450 °C. Further details on growth and sample characterization can be found in Ref. [51]. For ARPES experiments the samples were transferred after growth into a UHV suitcase in which they were transported to the ARPES station at the synchrotron without breaking UHV conditions.

Single crystal growth. For the growth of bulk MnTe crystals, pure manganese (99.9998 %) and tellurium (99.9999 %) in the molar composition $\text{Mn}_{33}\text{Te}_{67}$ were placed in an alumina (99.95 %) crucible and, together with a catch crucible filled with quartz wool, sealed in a fused silica tube under vacuum. The sample was first heated up to 1050 °C and then cooled down to 760 °C for four days. At 760 °C, the sample was quickly put into a centrifuge where the crystals were separated from the remaining melt. The crystals were in forms of flat plates with lateral dimensions of several millimeters and thicknesses of hundreds of micrometers.

Characterization. Single crystal X-ray diffraction measurements were performed with a Rigaku Smartlab with 9 kW Cu rotating anode, Ge two-bounce monochromator and Hypix detector. Powder diffraction measurements for the lattice parameter determination were performed using a Panalytical Empyrean with Cu-tube in Bragg-Brentano geometry. Powder diffraction simulations were performed using *xrayutilities* tool for reciprocal space conversion of scattering data [53]. Magnetometry measurements were performed in a Quantum

Design SQUID magnetometer using reciprocating sample option for increased measurement sensitivity. Temperature-dependent susceptibility measurements were taken in magnetic field of 50 mT. Note that for the X-ray diffraction and SQUID magnetometry investigations samples were cleaned in aqua regia to remove a parasitic MnTe_2 phase formed at the surface during the final phases of the growth. No traces of this phase could be detected in the X-ray diffraction investigations of the single crystals after this cleaning procedure. After cleaving the MnTe platelets therefore also expose a pristine α -MnTe (0001) surface.

Photoelectron spectroscopy. Angle-resolved photoemission spectroscopy (ARPES) was used for investigating the electronic structure of MnTe - including the Fermi surface, band structure, and one-electron spectral function $A(\omega, k)$ - which are resolved in electron momentum k (see Ref. [54] for more details). The extension of photon energies into the soft X-ray range (SX-ARPES) from a few hundred eV to approximately 2 keV enhances the probing depth of this technique, characterised by the photoelectron escape depth λ , by a factor of 3-5 compared to the conventional vacuum ultraviolet photon energies (UV-ARPES). This enables access to the intrinsic bulk properties, which is essential for three-dimensional (3D) materials like MnTe. The increase of λ reduces the intrinsic broadening δk_z of the out-of-plane momentum k_z , defined by the Heisenberg uncertainty principle as $\delta k_z \approx \lambda^{-1}$ [55]. Combined with the free-electron dispersion of high-energy final states, the resulting precise definition of k_z allows accurate determination of the 3D electronic structure. As in the case of MnTe, this advantage of SX-ARPES has been demonstrated, e.g., also on ferroelectric Rashba semiconductors [56], transition-metal dichalcogenides [55, 57], high-fold chiral fermion systems [58], etc.

The SX-ARPES experiments were conducted in the photon energy range 350-700 eV at the SX-ARPES end-station [59] of the ADRESS beamline at the Swiss Light Source, Paul Scherrer Institute, Switzerland [60]. All presented data were acquired with π -polarized X-rays. The photoelectrons were detected using the PHOIBOS-150 analyzer with an angular resolution of $\approx 0.1^\circ$ and using a deflector mode without changing the sample angles. The combined (beamline and analyzer) energy resolution varied between 50 and 100 meV in the above energy range. The experiments were performed in a vacuum of better than 1×10^{-10} mBar and at a sample temperature of around 15 K. The investigated MnTe thin film samples were transferred from the MBE in JKU Linz using a vacuum suitcase. In the presented data, the coherent spectral fraction was enhanced by subtracting the angle-integrated

spectral intensity as seen in Fig. 2a-c of main text. The constant energy-surface maps were integrated within a range of ± 50 meV. The conversion of the measured photoelectron kinetic energies and emission angles to binding energies and momenta was accomplished using the kinematic formulas which account for the photon momentum [59].

The spin-resolved ARPES (SARPES) measurements were conducted at 24 eV at COPHEE experimental station at the Swiss Light Source SIS beamline [61, 62] on *in situ* cleaved bulk single crystals at 21 K. Combined with an angle-resolving photoelectron spectrometer it produces complete data sets consisting of photoemission intensities (Fig. 4e), as well as spin polarization curves (Fig. 4g) with the combined experimental resolution of ≈ 25 meV and ≈ 100 meV, respectively.

Calculations. The experimental results were compared with *ab initio* electronic structure calculations, performed for MnTe in $P6_3/mmc$ (Space group:194) symmetry using the lattice parameter as determined from the XRD measurements [51].

We calculated the electronic structure of MnTe in Fig. 1 and 2 with the pseudo-potential density functional theory code Vienna Ab initio Simulation Package (VASP) [63]. We used Perdew-Burke-Ernzerhof (PBE) [64]+SOC+U, a spherically invariant type of Hubbard parameter [25] with a $8 \times 8 \times 5$ k-point grid, and a 520 eV energy cut-off.

The calculations in Fig. 2, 3 and 4 were carried out using spin-polarized fully relativistic Korringa-Kohn-Rostoker (SPRKKR) Green's function method in the atomic sphere approximation, within the rotationally invariant GGA+U scheme as implemented in the SPRKKR formalism [65, 66]. The screened on-site Coulomb interaction U and exchange interaction J of Mn are set to 4.80 eV and 0.80 eV respectively. The angular momentum expansion of the s, p, d, f orbital wave-functions has been used for each atom on a $28 \times 28 \times 15$ k -point grid. The energy convergence criterion has been set to 10^{-5} Ry. Lloyd's formula has been employed for accurate determination of the Fermi level [66–68].

The photoemission calculations for a semi-infinite surface of MnTe(001) with Mn atoms as the termination layer at the surface were performed within the one-step model of photoemission in the spin-density-matrix formulation as implemented in the SPRKKR package [69].

ACKNOWLEDGEMENT

We acknowledge fruitful discussions with Karel Výborný. This work was supported by the Czech Science Foundation project no. 19-28375X, Ministry of Education of the Czech Republic Grants LNSM-LNSpin, LM2018140, and the Neuron Endowment Fund Grant. L.S. acknowledges support from JGU TopDyn initiative. L.S. and J.S. acknowledge the funding by the Deutsche Forschungsgemeinschaft (DFG) Grant No. TRR 173 268565370 (project A03). S.W.D and J.M thanks CEDAMNF project financed by the Ministry of Education, Youth and Sports of Czech Republic, Project No. CZ.02.1.01/0.0/0.0/15 003/0000358 and CZ.02.01.01/00/22 008/0004572, co-funded by the ERDF. WRP acknowledges support from the Swiss National Science Foundation (Projects No. 200021-185037). K.U. acknowledges the program of Czech Research Infrastructures (project no. LM2023065). D.K. acknowledges the support from the Czech Academy of Sciences (project no. LQ100102201) and Czech Science Foundation (project no. 22-22000M) M.H. and G.S. would like to acknowledge support by the Austrian Science Funds, Project P30960-N27 and I-4493-N.

-
- [1] Kramers, H. A. Théorie générale de la rotation paramagnétique dans les cristaux. *Proc. Amsterdam Acad.* **33** (1930). URL <https://www.dwc.knaw.nl/DL/publications/PU00015981.pdf>.
- [2] Wigner, E. Ueber die Operation der Zeitumkehr in der Quantenmechanik. *Nachrichten von der Gesellschaft der Wissenschaften zu Göttingen, Mathematisch-Physikalische Klasse* **1932**, 546–559 (1932). URL <http://www.digizeitschriften.de/dms/img/?PPN=GDZPPN002509032>.
- [3] Chappert, C., Fert, A. & Van Dau, F. N. The emergence of spin electronics in data storage. *Nature Materials* **6**, 813–823 (2007). 1003.4058.
- [4] Ralph, D. C. & Stiles, M. D. Spin transfer torques. *Journal of Magnetism and Magnetic Materials* **320**, 1190–1216 (2008). 0711.4608.
- [5] Bader, S. D. & Parkin, S. Spintronics. *Annual Review of Condensed Matter Physics* **1**, 71–88 (2010). URL <http://www.annualreviews.org/doi/10.1146/annurev-conmatphys-070909-104123>.
- [6] Bhatti, S. *et al.* Spintronics based random access memory: a review. *Materials Today* **20**, 530–548 (2017). URL <https://linkinghub.elsevier.com/retrieve/pii/S1369702117304285>.
- [7] Manchon, A. *et al.* Current-induced spin-orbit torques in ferromagnetic and antiferromagnetic systems. *Reviews of Modern Physics* **91**, 035004 (2019). URL <https://link.aps.org/doi/10.1103/RevModPhys.91.035004>. 1801.09636.
- [8] Nagaosa, N., Sinova, J., Onoda, S., MacDonald, A. H. & Ong, N. P. Anomalous Hall effect. *Reviews of Modern Physics* **82**, 1539–1592 (2010). URL <https://link.aps.org/doi/10.1103/RevModPhys.82.1539>. 0904.4154.
- [9] Franz, M. & Molenkamp, L. (eds.) *Contemporary Concepts of Condensed Matter Science, vol. 6 - Topological Insulators* (Elsevier, 2013).
- [10] Bradlyn, B. *et al.* Topological quantum chemistry. *Nature* **547**, 298–305 (2017). URL <http://www.nature.com/articles/nature23268>. 1703.02050.
- [11] Šmejkal, L., Mokrousov, Y., Yan, B. & MacDonald, A. H. Topological antiferromagnetic spintronics. *Nature Physics* **14**, 242–251 (2018). URL <http://arxiv.org/abs/1706.00670>
<http://www.nature.com/articles/s41567-018-0064-5>. 1706.00670.

- [12] Zang, J., Cros, V. & Hoffmann, A. (eds.) *Topology in Magnetism*, vol. 192 of *Springer Series in Solid-State Sciences* (Springer International Publishing, Cham, 2018). URL <http://link.springer.com/10.1007/978-3-319-97334-0>.
- [13] Tokura, Y., Yasuda, K. & Tsukazaki, A. Magnetic topological insulators. *Nature Reviews Physics* **1**, 126–143 (2019). URL <http://www.nature.com/articles/s42254-018-0011-5>.
- [14] Vergniory, M. G. *et al.* A complete catalogue of high-quality topological materials. *Nature* **566**, 480–485 (2019). URL <https://doi.org/10.1038/s41586-019-0954-4><http://www.nature.com/articles/s41586-019-0954-4>.
- [15] Xu, Y. *et al.* High-throughput calculations of magnetic topological materials. *Nature* **586**, 702–707 (2020). URL <http://dx.doi.org/10.1038/s41586-020-2837-0>.
- [16] Elcoro, L. *et al.* Magnetic topological quantum chemistry. *Nature Communications* **12**, 5965 (2021). URL <http://dx.doi.org/10.1038/s41467-021-26241-8><https://www.nature.com/articles/s41467-021-26241-8>. 2010.00598.
- [17] Šmejkal, L., MacDonald, A. H., Sinova, J., Nakatsuji, S. & Jungwirth, T. Anomalous Hall antiferromagnets. *Nature Reviews Materials* **7**, 482–496 (2022). URL <http://arxiv.org/abs/2107.03321><https://www.nature.com/articles/s41578-022-00430-3>. 2107.03321.
- [18] Landau, L. & Lifshitz, E. *Electrodynamics of Continuous Media*, vol. 8 of *Course of Theoretical Physics* (Pergamon Press, Oxford, 1965), 2nd edn.
- [19] Winkler, R. *Spin–Orbit Coupling Effects in Two-Dimensional Electron and Hole Systems*, vol. 191 of *Springer Tracts in Modern Physics* (Springer Berlin Heidelberg, Berlin, Heidelberg, 2003). URL <http://link.springer.com/10.1007/b13586>.
- [20] Armitage, N. P., Mele, E. J. & Vishwanath, A. Weyl and Dirac semimetals in three-dimensional solids. *Reviews of Modern Physics* **90**, 015001 (2018). URL <https://link.aps.org/doi/10.1103/RevModPhys.90.015001>. 1705.01111.
- [21] Krempaský, J. *et al.* Disentangling bulk and surface rashba effects in ferroelectric α -gete. *Physical Review B* **94**, 205111 (2016). URL <https://journals.aps.org/prb/abstract/10.1103/PhysRevB.94.205111>.
- [22] Sante, D. D., Barone, P., Bertacco, R. & Picozzi, S. Electric control of the giant rashba effect in bulk gete. *Advanced Materials* **25**, 509–513 (2013).
- [23] Šmejkal, L., Sinova, J. & Jungwirth, T. Beyond Conventional Ferromagnetism and Antiferromagnetism: A Phase with Nonrelativistic Spin and Crystal Rotation Symmetry. *Physical*

- Review X* **12**, 031042 (2022). URL <https://link.aps.org/doi/10.1103/PhysRevX.12.031042>.
- [24] Šmejkal, L., Sinova, J. & Jungwirth, T. Emerging Research Landscape of Altermagnetism. *Physical Review X* **12**, 040501 (2022). URL <https://link.aps.org/doi/10.1103/PhysRevX.12.040501>. 2204.10844.
- [25] Gonzalez Betancourt, R. D. *et al.* Spontaneous Anomalous Hall Effect Arising from an Unconventional Compensated Magnetic Phase in a Semiconductor. *Physical Review Letters* **130**, 036702 (2023). URL <https://arxiv.org/abs/2112.06805v1><https://link.aps.org/doi/10.1103/PhysRevLett.130.036702>. 2112.06805.
- [26] Mazin, I. I. Altermagnetism in MnTe: origin, predicted manifestations, and routes to detwinning. *Physical Review B* **107**, L100418 (2023). URL <http://arxiv.org/abs/2301.08573>. 2301.08573.
- [27] Néel, L. Magnetism and Local Molecular Field. *Science* **174**, 985–992 (1971). URL <http://www.sciencemag.org/cgi/doi/10.1126/science.174.4013.985><http://www.ncbi.nlm.nih.gov/pubmed/17757022>.
- [28] Kunitomi, N., Hamaguchi, Y. & Anzai, S. Neutron diffraction study on manganese telluride. *Journal de Physique* **25**, 568–574 (1964). URL <http://www.edpsciences.org/10.1051/jphys:01964002505056800>.
- [29] Šmejkal, L., Železný, J., Sinova, J. & Jungwirth, T. Electric Control of Dirac Quasiparticles by Spin-Orbit Torque in an Antiferromagnet. *Physical Review Letters* **118**, 106402 (2017). URL <https://link.aps.org/doi/10.1103/PhysRevLett.118.106402>. 1610.08107.
- [30] Naka, M. *et al.* Spin current generation in organic antiferromagnets. *Nature Communications* **10**, 4305 (2019). URL <http://dx.doi.org/10.1038/s41467-019-12229-y><http://www.nature.com/articles/s41467-019-12229-y><https://doi.org/10.1038/s41467-019-12229-y>. 1902.02506.
- [31] González-Hernández, R. *et al.* Efficient Electrical Spin Splitter Based on Non-relativistic Collinear Antiferromagnetism. *Physical Review Letters* **126**, 127701 (2021). URL <http://arxiv.org/abs/2002.07073><https://link.aps.org/doi/10.1103/PhysRevLett.126.127701>. 2002.07073.
- [32] Naka, M., Motome, Y. & Seo, H. Perovskite as a spin current generator. *Physical Review B* **103**, 125114 (2021). URL <https://link.aps.org/doi/10.1103/PhysRevB.103.125114>.

2011.12459.

- [33] Ma, H.-Y. *et al.* Multifunctional antiferromagnetic materials with giant piezomagnetism and noncollinear spin current. *Nature Communications* **12**, 2846 (2021). URL <https://doi.org/10.1038/s41467-021-23127-7><http://www.nature.com/articles/s41467-021-23127-7>.
- [34] Šmejkal, L., Hellenes, A. B., González-Hernández, R., Sinova, J. & Jungwirth, T. Giant and Tunneling Magnetoresistance in Unconventional Collinear Antiferromagnets with Nonrelativistic Spin-Momentum Coupling. *Physical Review X* **12**, 011028 (2022). URL <https://link.aps.org/doi/10.1103/PhysRevX.12.011028>. 2103.12664.
- [35] Šmejkal, L., González-Hernández, R., Jungwirth, T. & Sinova, J. Crystal time-reversal symmetry breaking and spontaneous Hall effect in collinear antiferromagnets. *Science Advances* **6**, eaaz8809 (2020). 1901.00445.
- [36] Samanta, K. *et al.* Crystal Hall and crystal magneto-optical effect in thin films of SrRuO₃. *Journal of Applied Physics* **127**, 213904 (2020). URL <https://doi.org/10.1063/5.0005017><http://aip.scitation.org/doi/10.1063/5.0005017>.
- [37] Naka, M. *et al.* Anomalous Hall effect in κ ganic antiferromagnets. *Physical Review B* **102**, 075112 (2020). URL <https://journals.aps.org/prb/pdf/10.1103/PhysRevB.102.075112><https://link.aps.org/doi/10.1103/PhysRevB.102.075112>.
- [38] Hayami, S. & Kusunose, H. Essential role of the anisotropic magnetic dipole in the anomalous Hall effect. *Physical Review B* **103**, L180407 (2021).
- [39] Mazin, I. I., Koepf, K., Johannes, M. D., González-Hernández, R. & Šmejkal, L. Prediction of unconventional magnetism in doped FeSb₂. *PNAS* **118**, e2108924118 (2021). URL <http://arxiv.org/abs/2105.06356>. 2105.06356.
- [40] Naka, M., Motome, Y. & Seo, H. Anomalous Hall effect in antiferromagnetic perovskites. *Physical Review B* **106**, 195149 (2022). URL <http://arxiv.org/abs/2208.11823><https://link.aps.org/doi/10.1103/PhysRevB.106.195149>. 2208.11823.
- [41] Feng, Z. *et al.* An anomalous Hall effect in altermagnetic ruthenium dioxide. *Nature Electronics* **5**, 735–743 (2022). URL <https://www.nature.com/articles/s41928-022-00866-z>.
- [42] Bose, A. *et al.* Tilted spin current generated by an antiferromagnet. *Nature Electronics* **5**, 263–264 (2022). URL <http://arxiv.org/abs/2108.09150><https://www.nature.com/articles/s41928-022-00758-2>. 2108.09150.

- [43] Bai, H. *et al.* Observation of Spin Splitting Torque in a Collinear Antiferromagnet RuO₂. *Physical Review Letters* **128**, 197202 (2022). URL <http://arxiv.org/abs/2109.05933><https://link.aps.org/doi/10.1103/PhysRevLett.128.197202>. 2109.05933.
- [44] Karube, S. *et al.* Observation of Spin-Splitter Torque in Collinear Antiferromagnetic RuO₂. *Physical Review Letters* **129**, 137201 (2022). URL <https://doi.org/10.1103/PhysRevLett.129.137201><https://link.aps.org/doi/10.1103/PhysRevLett.129.137201>. 2111.07487.
- [45] Strocov, V. N. *et al.* High-resolution soft x-ray beamline address at the swiss light source for resonant inelastic x-ray scattering and angle-resolved photoelectron spectroscopies. *Journal of Synchrotron Radiation* **17**, 631–643 (2010).
- [46] Strocov, V. N. *et al.* Soft-x-ray arpes facility at the adress beamline of the sls: Concepts, technical realisation and scientific applications. *Journal of Synchrotron Radiation* **21**, 32–44 (2014).
- [47] Kriegner, D. *et al.* Multiple-stable anisotropic magnetoresistance memory in antiferromagnetic MnTe. *Nature Communications* **7**, 11623 (2016). 1508.04877.
- [48] Ebert, H., Ködderitzsch, D. & Minár, J. Calculating condensed matter properties using the KKR-Green’s function method—recent developments and applications. *Reports on Progress in Physics* **74**, 096501 (2011). URL <https://iopscience.iop.org/article/10.1088/0034-4885/74/9/096501>.
- [49] Braun, J., Minár, J. & Ebert, H. Correlation, temperature and disorder: Recent developments in the one-step description of angle-resolved photoemission. *Physics Reports* **740**, 1–34 (2018).
- [50] Zhang, P. *et al.* A precise method for visualizing dispersive features in image plots. *Review of Scientific Instruments* **82** (2011). URL <https://pubs.aip.org/rsi/article/82/4/043712/353698/A-precise-method-for-visualizing-dispersive>. 1104.1524.
- [51] Kriegner, D. *et al.* Magnetic anisotropy in antiferromagnetic hexagonal MnTe. *Physical Review B* **96**, 214418 (2017). URL <https://link.aps.org/doi/10.1103/PhysRevB.96.214418>. 1710.08523.
- [52] Hoesch, M. *et al.* Spin-polarized fermi surface mapping (2002). URL www.elsevier.com/locate/elspec.
- [53] Kriegner, D., Wintersberger, E. & Stangl, J. Xrayutilities: A versatile tool for reciprocal space conversion of scattering data recorded with linear and area detectors. *Journal of Applied Crystallography* **46**, 1162 (2013).

- [54] Damascelli, A., Hussain, Z. & Shen, Z.-X. Angle-resolved photoemission studies of the cuprate superconductors. *Rev. Mod. Phys.* **75**, 473–541 (2003). URL <https://link.aps.org/doi/10.1103/RevModPhys.75.473>.
- [55] Strocov, V. N. *et al.* Three-dimensional electron realm in VSe_2 by soft-x-ray photoelectron spectroscopy: Origin of charge-density waves. *Phys. Rev. Lett.* **109**, 086401 (2012). URL <https://link.aps.org/doi/10.1103/PhysRevLett.109.086401>.
- [56] Krempaský, J. *et al.* Disentangling bulk and surface Rashba effects in ferroelectric α -GeTe. *Phys. Rev. B* **94**, 205111 (2016).
- [57] Weber, F. *et al.* Three-dimensional fermi surface of $2h$ -NbSe₂: Implications for the mechanism of charge density waves. *Phys. Rev. B* **97**, 235122 (2018). URL <https://link.aps.org/doi/10.1103/PhysRevB.97.235122>.
- [58] Schröter, N. *et al.* Observation and control of maximal chern numbers in a chiral topological semimetal. *Science* **369**, 179–183 (2020).
- [59] Strocov, V. N. *et al.* Soft-X-ray ARPES facility at the ADDRESS beamline of the SLS: concepts, technical realisation and scientific applications. *Journal of Synchrotron Radiation* **21**, 32–44 (2014).
- [60] Strocov, V. N. *et al.* High-resolution soft X-ray beamline ADDRESS at the Swiss Light Source for resonant inelastic X-ray scattering and angle-resolved photoelectron spectroscopies. *Journal of Synchrotron Radiation* **17**, 631–643 (2010).
- [61] Hoesch, M. *et al.* Spin-polarized fermi surface mapping. *Journal of Electron Spectroscopy and Related Phenomena* **124**, 263 – 279 (2002). URL <http://www.sciencedirect.com/science/article/B6TGC-45JH0V9-6/2/0a0d8bba99ba30730b60463fc5ca2baf>.
- [62] Dil, J. H. Spin and angle resolved photoemission on non-magnetic low-dimensional systems. *Journal of Physics: Condensed Matter* **21**, 403001 (2009).
- [63] Kresse, G. & Furthmüller, J. Efficient iterative schemes for ab initio total-energy calculations using a plane-wave basis set. *Physical Review B* **54**, 11169–11186 (1996). 0927-0256(96)00008.
- [64] Perdew, J. P., Burke, K. & Ernzerhof, M. Generalized gradient approximation made simple. *Physical Review Letters* **78**, 1396–1396 (1996). URL <https://link.aps.org/doi/10.1103/PhysRevLett.78.1396>. 0927-0256(96)00008.
- [65] Ebert, H., Ködderitzsch, D. & Minár, J. Calculating condensed matter properties using the KKR-Green’s function method—recent developments and applications. *Rep. Prog. Phys.* **74**

- (2011).
- [66] Minár, J. Correlation effects in transition metals and their alloys studied using the fully self-consistent kkr-based lsda + dmft scheme. *Journal of Physics: Condensed Matter* **23**, 253201 (2011).
- [67] Lloyd, P. Wave propagation through an assembly of spheres: Ii. the density of single-particle eigenstates. *Proceedings of the Physical Society* **90**, 207 (1967). URL <https://dx.doi.org/10.1088/0370-1328/90/1/323>.
- [68] Lloyd, P. & Smith, P. Multiple scattering theory in condensed materials. *Advances in Physics* **21**, 69–142 (1972).
- [69] Braun, J., Minár, J. & H., E. Correlation, temperature and disorder: Recent developments in the one-step description of angle-resolved photoemission. *Physics Reports* **740**, 1–34 (2018).